

# Benchmarking Quantum Data Center Architectures: A Performance and Scalability Perspective

Shahrooz Pouryousef  
Quantum Lab, Cisco Research  
USA

Don Towsley  
University of Massachusetts  
Amherst, USA

Eneet Kaur  
Quantum Lab, Cisco Research  
USA

Ramana Kompella  
Quantum Lab, Cisco Research  
USA

Hassan Shapourian  
Quantum Lab, Cisco Research  
USA

Reza Nejabati  
Quantum Lab, Cisco Research  
USA

## Abstract

Scalable distributed quantum computing (DQC) has motivated the design of multiple quantum data-center (QDC) architectures that overcome the limitations of single quantum processors through modular interconnection. While these architectures adopt fundamentally different design philosophies, their relative performance under realistic quantum hardware constraints remains poorly understood.

In this paper, we present a systematic benchmarking study of four representative QDC architectures—QFly, BCube, Clos, and Fat-Tree—quantifying their impact on distributed quantum circuit execution latency, resource contention, and scalability. Focusing on quantum-specific effects absent from classical data-center evaluations, we analyze how optical-loss-induced Einstein–Podolsky–Rosen (EPR) pair generation delays, coherence-limited entanglement retry windows, and contention from teleportation-based non-local gates shape end-to-end execution performance. Across diverse circuit workloads, we evaluate how architectural properties such as path diversity and path length, and shared BSM (Bell State Measurement) resources interact with optical-switch insertion loss and reconfiguration delay. Our results show that distributed quantum performance is jointly shaped by topology, scheduling policies, and physical-layer parameters, and that these factors interact in nontrivial ways. Together, these insights provide quantitative guidance for the design of scalable and high-performance quantum data-center architectures for DQC.

## 1 Introduction

Distributed Quantum Computing (DQC) has emerged as a promising approach for scaling quantum systems beyond the limits of single quantum processors by interconnecting multiple smaller Quantum Processing Units (QPUs) through quantum networks [6, 25, 26, 32]. In DQC, circuits are partitioned across QPUs, and non-local operations are executed using entanglement-assisted primitives such as gate or state teleportation. Recent experimental demonstrations across multiple qubit platforms have validated the feasibility of such

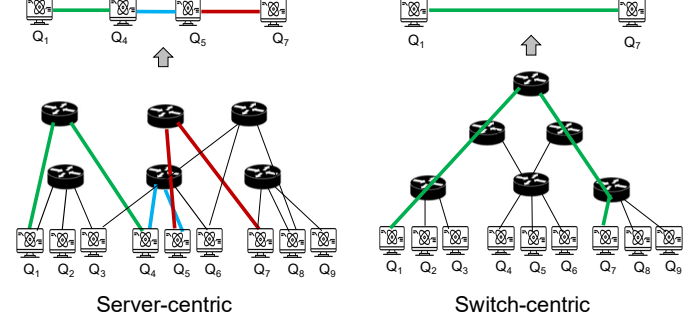


**Figure 1: Entanglement routing in server-centric architectures using QPUs as repeaters versus switch-centric optical switching architectures.**

non-local operations [21, 27], while compiler and orchestration frameworks based on lattice surgery and distributed surface codes for error correction have further advanced fault-tolerant distributed quantum computing [8, 12, 16, 30, 32].

To support DQC at scale, several quantum data-center (QDC) architectures have been proposed, many inspired by classical data-center topologies but adapted to quantum networking constraints. These architectures emphasize different design goals, such as minimizing path length (e.g., Qfly [25]) or maximizing path diversity (e.g., Fat-tree [26]). In the classical domain, such topologies have been extensively benchmarked using metrics including throughput, fault tolerance, and capital efficiency [20, 23, 31]. However, a comparable, cross-architectural evaluation remains largely absent in the quantum setting.

While both classical and quantum data-center benchmarking must consider factors beyond topology, QDC benchmarking introduces additional quantum-specific constraints that are absent in classical settings. In particular, distributed execution depends on stochastic entanglement generation subject to optical loss, coherence-limited retry windows for communication qubits, and teleportation-based non-local gates that contend for shared Bell-state measurement modules

(BSMs) and detector resources. These effects interact non-linearly with architectural properties, including switch hierarchy, path length between QPUs, available path diversity, and the distribution of shared photonic resources. As a result, improvements in individual hardware parameters—such as reduced switch insertion loss, faster reconfiguration of optical switches when establishing photonic paths between different QPU pairs, or increased communication-qubit availability—do not translate uniformly into system-level gains. Understanding when performance is dominated by topology, by resource contention, or by physical-layer limitations remains an open question.

Figure 1 illustrates how quantum-specific constraints arise from the physical realization of quantum interconnects and shape how entanglement is established between QPUs. In *server-centric* architectures such as BCube, communication paths form repeater chains in which intermediate QPUs actively perform entanglement swapping, introducing and causing latency and noise to accumulate across multiple hops and making EPR generation sensitive to scheduling under finite coherence windows [19, 24]. In contrast, *switch-centric* architectures route entanglement through the optical switching fabric, where QPUs act only as endpoints and swapping is performed at BSM-capable switches along the path. In this figure, for both cases, we abstract each non-local operation as consuming a single *virtual entanglement link* between the communicating QPUs, which aggregates physical losses and operational imperfections.

In this work, we present a systematic benchmarking of four representative QDC architectures—QFly [25], BCube [26], Clos [26], and Fat-Tree [26]—under diverse circuit workloads and physical-layer conditions. Our evaluation explicitly examines how architectural design choices affect (i) end-to-end circuit execution latency under realistic entanglement-generation models, (ii) the number of switch hops incurred by non-local gates, and (iii) contention for BSM resources. We study multiple architectural variants to isolate the trade-offs between path length, contention, and scalability. Workloads span a range of circuit widths and depths, connectivity patterns, and two-qubit gate densities, enabling us to assess how algorithmic structure interacts with architectural and physical constraints.

Our study yields several architecture-level insights for designing scalable QDCs. First, performance is tightly coupled to how BSM resources are provisioned. Under a fixed *per-switch* BSM capacity model, architectures with a larger number of switches and greater path diversity—such as Clos and Fat-Tree—achieve lower latency by exposing a higher aggregate BSM pool and enabling more parallel entanglement generation across the network. In contrast, when switching to a fixed *total* BSM budget across the entire fabric, architectures with fewer switches and shorter end-to-end paths

benefit disproportionately: reduced hop counts and lower accumulated optical loss allow switch-light designs to achieve faster EPR generation despite a smaller number of fabric elements. Second, BCube exposes an additional coherence-driven trade-off: increasing the communication-memory cut-off  $\tau_{\text{cut}}$  steadily improves BCube latency. Third, sensitivity to optical switch insertion loss is strongly topology dependent. In Clos and Fat-Tree, remote entanglement traverses many optical switches, causing loss to accumulate across hops and latency to increase rapidly as per-switch loss grows. In contrast, QFly and BCube are less sensitive due to shorter paths and, for BCube, the use of QPUs as repeaters that do not incur switch insertion loss in our model. Together, these results show that topology, resource placement, and physical-layer parameters interact nontrivially, motivating architecture-aware benchmarking for DQC.

The remainder of this paper is organized as follows. Section § 2 introduces the architectural characteristics and photonic components of each QDC topology. Section § 3 presents our simulation methodology and evaluation results. Section 4 discusses design implications and future directions for co-optimizing topology, scheduling, and physical-layer control in scalable quantum data centers.

## 2 Data Center Network Designs

This section presents the architectural principles, parameterization, and scaling behavior of the four quantum data-center architectures evaluated in this work: Fat-Tree, Clos, QFly, and BCube. We focus on structural properties that directly influence scalability, path diversity, switch count, and the role of QPUs in communication, together with a high-level physical-layer loss and entanglement-timing model.

Distributed quantum computing performance depends on multiple factors, including circuit partitioning [3, 5, 14], compiler transformations (e.g., circuit rewrites that adapt programs to architectural constraints and reduce non-local communication) [16], and entanglement-generation and scheduling policies [13, 22]. Modeling all such interactions jointly is beyond the scope of this work. Instead, our objective is to establish a controlled architectural baseline that isolates the impact of network topology and shared photonic resources on distributed execution.

In this paper, we use the term fabric to denote the optical interconnection network—including switches, links, and Bell-state measurement resources that establishes and routes entanglement between QPUs.

### 2.1 QDC Hardware Components and Entanglement Generation

We summarize the core hardware components common to quantum data-center (QDC) architectures and describe the

entanglement-generation abstraction used throughout this work.

Each QPU comprises a collection of *data qubits*, which store and process algorithmic quantum state, and a smaller number of *communication qubits*, which interface with the photonic fabric to establish remote entanglement. Communication qubits are required because entanglement is generated and heralded outside the QPU — via photonic interference and detection — must be coherently mapped onto local matter qubits before it can be consumed by computation. Non-local two-qubit operations between QPUs are executed using entanglement-assisted primitives, most commonly *gate teleportation* or *state teleportation*, which consume pre-shared EPR pairs together with local operations and classical communication. Compared to local gates, these primitives incur additional latency and resource consumption, as they depend on successful entanglement generation, Bell-state measurements, and timely classical coordination. As a result, the availability and scheduling of communication qubits, as well as contention for shared photonic resources, directly shape the performance of distributed quantum execution.

A typical QDC optical fabric consists of the following building blocks: (i) *entangled photon-pair sources (EPPS)*, which probabilistically generate pairs of entangled photons; (ii) *optical switches (OSWs)*, which configure photonic paths across racks, groups, or switching stages; (iii) *Bell-state measurement modules (BSMs)*, which perform two-photon interference and herald successful entanglement generation or entanglement swapping; and (iv) *single-photon detectors (SPDs)*, often operated cryogenically to reduce dark counts and timing jitter. Each QPU connects to the optical fabric through a limited number of optical I/O ports; to increase concurrency, multiple communication qubits may share a port via time-division multiplexing (TDM) or wavelength-division multiplexing (WDM), at the cost of synchronization and control overhead. In addition to these quantum components, QDC operation relies on a classical control plane that provides clock distribution, phase stabilization, heralding signals, and feedforward communication, which together enable coordinated entanglement generation and distributed gate execution.

*Entanglement-generation protocol.* In this work, we focus on a *scatter–scatter* (midpoint-interference) entanglement-generation protocol, which is representative of near-term photonic quantum networks and is widely adopted in experimental and architectural studies. Alternative protocols—such as memory–memory or memory–source links—are discussed extensively in the literature (e.g., [4]) and are left for future exploration.

As illustrated schematically in Fig. 2, the scatter–scatter protocol employs two independent entangled photon-pair

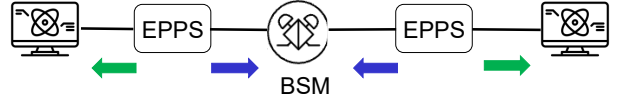


**Figure 2: Scatter–scatter entanglement generation using independent (possibly non-degenerate) photon-pair sources and a central BSM.**

sources placed within the optical fabric. During each entanglement attempt, one photon from each pair is routed toward a central BSM, while the corresponding partner photons propagate toward the two endpoint QPUs and interact with their respective communication qubits. A successful end-to-end entanglement event is heralded by a coincidence detection at the BSM together with the appropriate scattering or absorption events at the two endpoint QPUs. Only upon these classical detection signals do the endpoint communication qubits share a heralded Bell pair.

A key advantage of this protocol is its compatibility with *non-degenerate* entanglement sources, which emit photon pairs at different wavelengths (e.g., near-infrared and telecom). This enables efficient interfacing between QPUs and low-loss optical fibers without relying on high-performance quantum frequency conversion at the endpoints. As a result, scatter–scatter links are well suited to heterogeneous photonic fabrics and near-term QDC deployments.

## 2.2 Switch-Centric vs. Server-Centric

QDC architectures can be broadly classified as *switch-centric* or *server-centric*, depending on where entanglement-generation, switching, and swapping operations are performed.

*Switch-centric architectures.* In a switch-centric design, QPUs are connected by a switching fabric: they emit or absorb photons but do not store or process intermediate entangled states. End-to-end entanglement across multiple hops is realized through optical path composition inside the fabric, typically requiring a single BSM operation per Bell pair. Fat-Tree, Clos, and QFly architectures fall into this category.

This design simplifies QPU requirements and avoids requiring long-lived quantum memory at intermediate nodes. However, it concentrates contention and loss within shared switching elements, making performance sensitive to switch port budgets, BSM availability, and reconfiguration delays.

*Server-centric architectures.* In server-centric designs, QPUs participate directly in entanglement distribution by acting as repeaters. Intermediate QPUs store entangled states and perform Bell-state measurements to extend entanglement over multiple hops. BCube exemplifies this approach.

**Table 1: Common notation used in the architecture overview.**

Symbol	Meaning
$N$	Number of QPUs (system size)
$k$	Port budget (ports per switch)
$T$	Number of ToR switches (Clos)
$R$	QPUs per rack (Clos)
$n$	BCube switch radix ( $n \triangleq k$ )
$k_{\text{bcube}}$	BCube level parameter
$k_{\text{ring}}$	QFly inter-switch degree
$N_{\text{rep}}$	# repeater QPUs on a BCube path

Compared to switch-centric architectures, server-centric designs trade reduced dependence on complex optical switching hardware for increased reliance on QPU capabilities. Multi-hop entanglement requires multiple Bell-state measurements and quantum memory hold times, making performance sensitive to communication-qubit coherence and scheduling efficiency.

This distinction has important system-level consequences. In a switch-centric design, each multi-hop optical path requires only a single BSM operation for an end-to-end Bell pair, whereas in a server-centric design, a repeater chain with  $N_{\text{rep}}$  intermediate QPUs requires  $N_{\text{rep}} + 1$  Bell-state measurements and corresponding storage intervals. These additional operations directly impact achievable entanglement rates, fidelity, and scheduling complexity, motivating the architectural comparisons studied in the remainder of this paper. This distinction parallels classical data-center networks, where switch-centric Clos fabrics treat servers as pure endpoints, while server-centric designs such as DCell and BCube involve servers directly in routing and forwarding decisions [10, 11]. Analogously, in quantum data centers, switch-centric architectures centralize entanglement operations in the fabric, whereas server-centric architectures allow QPUs to participate in entanglement distribution.

*Notation.* Table 1 summarizes the notation used throughout the paper. We use  $N$  to denote the total number of QPUs in the system. Each optical switch has a fixed *port budget*  $k$ , also referred to as the *switch radix*, which specifies the total number of input/output ports available on the switch for connecting QPUs or other switches. For Clos-style architectures,  $T$  denotes the number of top-of-rack (ToR) switches, where a rack is a physical grouping of co-located QPUs and a ToR switch aggregates and connects all QPUs within a single rack;  $R$  denotes the number of QPUs attached to each rack.

For BCube, we consider a server-centric design in which QPUs participate in routing; the BCube switch radix is set to  $n \triangleq k$ , and  $k_{\text{bcube}}$  denotes the BCube *level parameter*, i.e., the

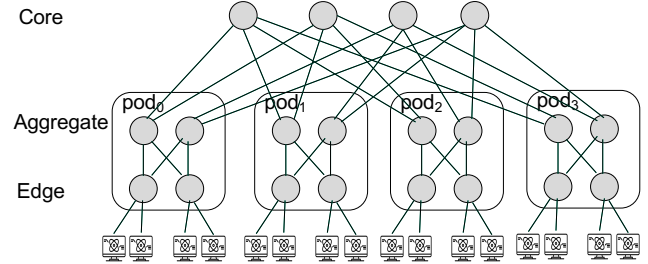


**Figure 3: A Fat-Tree architecture with pods.** Each of the  $k$  pods contains  $k/2$  edge (top-of-rack) and  $k/2$  aggregation switches that connect QPUs to a shared core layer of  $(k/2)^2$  switches, providing full bisection bandwidth under uniform switch radix  $k$ .

number of switch layers in the BCube topology, which determines the network depth and path diversity. For QFly,  $k_{\text{ring}}$  denotes the inter-switch degree, i.e., the number of ports on each switch allocated to connections with other switches, under the same total port budget  $k$ . Finally, for server-centric (BCube) routing,  $N_{\text{rep}}$  denotes the number of intermediate repeater QPUs traversed along a communication path between two endpoint QPUs.

### 2.3 Fat-Tree Architecture

Fat-Tree is a canonical *switch-centric* data-center network originally proposed in the classical networking literature to provide full bisection bandwidth (i.e., sufficient aggregate interconnect capacity to support simultaneous full-rate communication between any equal partition of endpoints), predictable routing, and high path diversity at scale [1, 18]. Its design philosophy is to realize high aggregate bandwidth using many moderate-radix switches arranged in a symmetric multi-tier hierarchy, rather than relying on expensive ultra-high-radix switches.

The Fat-Tree fabric is organized into three logical layers as shown in figure 3: edge (top-of-rack), aggregation, and core. QPUs connect to top-of-rack switches. Edge switches aggregate intra-rack traffic, aggregation switches provide connectivity among racks within a pod, and core switches interconnect pods. QPUs attach to edge switches via dedicated access ports. This regular hierarchy yields a symmetric topology with uniform path lengths and balanced bandwidth, enabling predictable routing and efficient load balancing.

*Parameterization and scaling.* We characterize a Fat-Tree by its switch radix  $k$ , representing the number of ports per switch. We choose  $k$  such that it is the smallest even value  $k \geq 2$  for which the resulting topology can accommodate

the target system size  $N$ :

$$k = \min \left\{ k' \in 2\mathbb{Z}_{\geq 2} : \frac{k'^3}{4} \geq N \right\}. \quad (1)$$

For a given  $k$ , the network comprises  $k$  pods, where each pod is a modular subnetwork containing  $k/2$  edge (top-of-rack) switches,  $k/2$  aggregation switches, and the QPUs attached to those edge switches. The network further includes a core layer of  $(k/2)^2 = k^2/4$  switches:

$$S_{\text{edge}} = \frac{k^2}{2}, \quad S_{\text{agg}} = \frac{k^2}{2}, \quad S_{\text{core}} = \frac{k^2}{4}, \quad S_{\text{total}} = \frac{5k^2}{4}. \quad (2)$$

Each edge switch serves up to  $k/2$  QPUs, which sets the maximum rack capacity to

$$H_{\text{per-edge}} = \frac{k}{2}. \quad (3)$$

This construction follows the canonical  $k$ -ary Fat-Tree topology of Al-Fares *et al.* [2].

## 2.4 Clos Architecture

Clos is a flexible *switch-centric* architecture that generalizes the Fat-Tree design by decoupling system scale from a single global radix parameter. While the canonical data-center Fat-Tree corresponds to a specific symmetric instantiation of a folded-Clos network, the broader Clos framework admits a wide range of valid realizations obtained by independently dimensioning switch radix, rack fanout, and fabric size. As in Fat-Tree, QPUs act strictly as endpoints and connect to a multi-stage optical switching fabric.

*High-level organization.* Clos networks employ a multi-stage switching fabric composed of top-of-rack (ToR), aggregation, and core layers. QPUs attach to ToR switches via dedicated access ports, while the remaining ports are used for inter-switch connectivity across stages. Unlike Fat-Tree, which enforces a fixed and symmetric relationship between the number of switches and port allocations, Clos allows these parameters to vary, enabling finer-grained control over rack density and overall fabric scale.

*Design flexibility.* A Clos fabric can be instantiated in infinitely many ways depending on how ToR fanout and switch radix are chosen. Given  $T$  ToR switches and  $R$  QPUs per ToR, the fabric supports up to  $T \times R$  QPUs. For a target system size  $N$ , any configuration satisfying  $T \times R \geq N$  is feasible, with the difference  $T \times R - N$  corresponding to *unused rack capacity*, i.e., unoccupied host attachment slots arising from rack-level granularity.

Different Clos designs reflect different architectural priorities. A *Clos\_tight* design emphasizes dense rack packing by selecting parameters that keep unused rack capacity minimal, resulting in closely matched fabric and system sizes. In contrast, a *Clos\_compact* design emphasizes reducing the total number of switches in the fabric, allowing modest unused rack capacity when doing so simplifies the switching

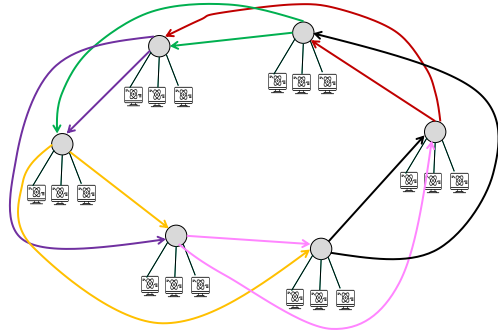


**Figure 4: Example QFly topology with  $S = 6$  switches, each serving  $m = 3$  QPUs ( $N = 18$ ). Each switch uses  $k_{\text{ring}} = 2$  ports for inter-switch connectivity. By increasing  $k_{\text{ring}}$  we can reduce the number of hops between QPUs.**

infrastructure. Both represent valid points within the broader Clos design space and share the same fundamental wiring principles.

*Implications.* Compared to Fat-Tree, Clos provides finer-grained control over system scaling and rack density without requiring a single global radix to determine capacity. This flexibility enables tighter matching between system size and physical resources, but introduces additional degrees of freedom that can increase switch count and coordination overhead depending on how the fabric is dimensioned.

## 2.5 QFly Architecture

QFly is a flattened, low-diameter *switch-centric* architecture inspired by Dragonfly-style interconnects, which employ groups of high-radix routers and sparse global links to achieve low diameter while limiting long-cable cost [17]. In QFly, QPUs are grouped under a smaller number of high-radix optical switches, reducing hierarchy depth and the number of fabric elements compared to Fat-Tree and Clos.

*Implications.* Increasing inter-switch connectivity reduces network diameter and increases path diversity, but concentrates traffic onto fewer high-radix switching elements.

## 2.6 BCube Architecture

BCube is a *server-centric* architecture in which QPUs connect to multiple switch layers and can participate directly in entanglement distribution. Unlike switch-centric designs, BCube can form end-to-end entanglement via *repeater chains*: intermediate QPUs generate, store, and swap EPR pairs on behalf of other QPUs, so QPUs serve dual roles as compute nodes and repeaters.

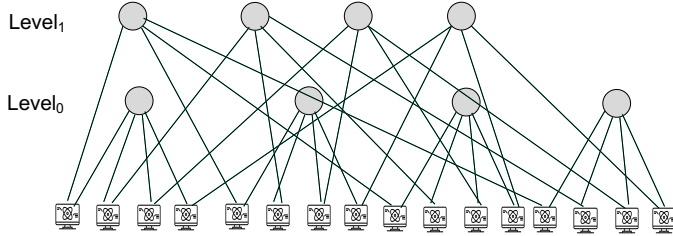


**Figure 5: Example (4, 2)-BCube topology with 16 QPUs. QPUs connect to two switch layers, with four switches per level. Communication paths may traverse intermediate QPUs, which act as repeaters in the server-centric BCube design.**

We follow the original BCube construction of Guo *et al.* [10]. An  $(n, k_{\text{bcube}})$ -BCube consists of  $k_{\text{bcube}} + 1$  switch layers, each containing  $n^{k_{\text{bcube}}}$  switches of radix  $n$ . Each QPU connects to exactly one switch in every layer, and the total system capacity scales as  $n^{k_{\text{bcube}}+1}$  QPUs as shown in figure 5.

QPUs are indexed by  $(k_{\text{bcube}} + 1)$ -digit identifiers in base  $n$ , and switch connectivity is defined by fixing one digit position per layer. As a result, when the number of instantiated QPUs is smaller than the full  $n^{k_{\text{bcube}}+1}$  capacity, only the subset of switches whose indices are referenced by at least one QPU are *active*, while the remaining switches are structurally present but unused. This distinction is important for accurately accounting for switch count, port utilization, and available Bell-state measurement (BSM) resources in partially populated BCube instances.

*Repeater-chain implications.* For a path with  $N_{\text{rep}}$  intermediate repeater QPUs, establishing an end-to-end Bell pair requires generating entanglement on  $N_{\text{rep}} + 1$  segments and performing  $N_{\text{rep}} + 1$  Bell-state measurements (one per swap).

## 2.7 Optical Loss and EPR-Generation Timing Model

We model the time required to generate entanglement in different architectures for non-local gates. A *non-local two-qubit gate* is a gate whose two operand qubits reside on different QPUs. To execute such a gate, a scheduler selects a *path* between the two endpoint QPUs and requests the generation of an Einstein–Podolsky–Rosen (EPR) pair along that path. For each non-local gate, we estimate the *expected* EPR-generation latency  $\mathbb{E}[T_{\text{pair}}]$  associated with the scheduler-selected path.

*paths and hop count.* A path is an ordered sequence of physical links connecting the two endpoint QPUs that host the operand qubits of a non-local gate. These links consist of

QPU–switch, switch–switch, and switch–QPU connections, depending on the architecture.

In switch-centric architectures (QFly, Clos, and Fat-Tree), QPUs act strictly as endpoints. A path starts with a QPU–switch link from the source QPU, traverses one or more switch–switch links within the optical switching network, and ends with a switch–QPU link to the destination QPU. Intermediate QPUs do not participate in entanglement distribution. Regardless of path length, a multi-hop path requires only a single Bell-state measurement (BSM) within the switching network to establish end-to-end entanglement.

In server-centric architectures (BCube), QPUs may act as repeaters. A path consists of a sequence of QPU–switch–QPU segments, where each intermediate QPU stores entanglement and performs entanglement swapping to extend the connection. As a result, entanglement is generated hop by hop: each adjacent QPU pair requires BSM capacity at the connecting switch, and each intermediate QPU must have available communication qubits.

*Per-attempt timing.* Entanglement is generated probabilistically through repeated attempts. Let  $T_{\text{att}}$  denote the duration of a single entanglement-generation attempt on a given path. We model

$$T_{\text{att}} = T_{\text{src}} + \frac{2D}{v_{\text{fiber}}} + T_{\text{reset}}, \quad (4)$$

where  $T_{\text{src}}$  is the source repetition time,  $T_{\text{reset}}$  is the communication-qubit reset or reinitialization time,  $v_{\text{fiber}}$  is the speed of light in fiber, and  $D$  is the total fiber length traversed by photons along the selected path.

*Optical loss model.* For a given path, the total optical loss (in dB) is modeled as

$$L_{\text{tot}} = L_{\text{fiber}} + L_{\text{sw}} + L_{\text{BSM}} (+ L_{\text{mem}}), \quad (5)$$

where  $L_{\text{fiber}}$  captures fiber attenuation,  $L_{\text{sw}}$  is the cumulative insertion loss from optical switches, and  $L_{\text{BSM}}$  abstracts inefficiencies in Bell-state measurement operations (e.g., coupling and detector loss). The term  $L_{\text{mem}}$  applies only to server-centric paths and captures additional loss due to storing entanglement in intermediate QPU memories, including photon–matter conversion loss and decoherence during storage.

*Switch insertion loss.* Photons traversing an optical switch incur insertion loss due to the internal multi-stage switching structure. With switch radix  $k$  and per- $2 \times 2$  element loss  $\ell_{2 \times 2}$  (dB), the loss of a single switch traversal is approximated as

$$L_{\text{sw}}(k) \approx (2 \lceil \log_2 k \rceil - 1) \ell_{2 \times 2},$$

corresponding to a Beneš-style non-blocking optical switch design [29]. Let  $n_{\text{sw}}$  denote the number of switch traversals along the path; then  $L_{\text{sw}} = n_{\text{sw}} L_{\text{sw}}(k)$ .

**Table 2: Notation for the optical loss and timing model.**

Symbol	Description
$h$	Number of hops in a path
$\ell$	Fiber length per segment (km)
$\alpha$	Fiber attenuation (dB/km)
$k$	Switch radix
$\ell_{2 \times 2}$	Loss of one $2 \times 2$ switch element (dB)
$L_{\text{fiber}}$	Total fiber loss (dB)
$L_{\text{sw}}$	Total switch insertion loss (dB)
$L_{\text{BSM}}$	Bell-state measurement loss (dB)
$L_{\text{mem}}$	Per-hop memory loss (dB)
$T_{\text{chan}}$	End-to-end transmittance
$T_{\text{coh}}$	Communication-qubit coherence cutoff
$\mathbb{E}[T_{\text{pair}}]$	Expected EPR-generation latency

*Expected EPR-generation latency.* Total loss is converted to an end-to-end transmittance  $T_{\text{chan}} = 10^{-L_{\text{tot}}/10}$ , which we interpret as the per-attempt success probability for generating an EPR pair along the selected path. For switch-centric architectures, assuming independent attempts, the expected EPR-generation latency is

$$\mathbb{E}[T_{\text{pair}}] \approx \frac{T_{\text{att}}}{T_{\text{chan}}}. \quad (6)$$

*Server-centric retry window and protocols.* In server-centric architectures such as BCube, entanglement must be generated on multiple segments and combined through entanglement swapping at intermediate QPUs. Because partially generated entanglement must be stored while waiting for other segments to succeed, we impose a coherence-limited *retry window*  $\tau_{\text{cut}}$ . If an end-to-end EPR pair has not been successfully formed via swapping within  $\tau_{\text{cut}}$ , the attempt is discarded and restarted. We evaluate two repeater-chain scheduling protocols—*sequential* and *parallel*—introduced in [24], which capture different trade-offs between control simplicity and latency. For these protocols, we estimate the raw end-to-end entanglement delivery rate  $R_{\text{raw}}$  and compute

$$\mathbb{E}[T_{\text{pair}}] \approx \frac{1}{R_{\text{raw}}}. \quad (7)$$

### 3 Evaluation

In this section, we evaluate multiple variants of the QFly, BCube, Fat-Tree, and Clos architectures using three targeted experiments. Each experiment isolates a specific physical or architectural factor that influences the execution latency of distributed quantum circuits.

*Workloads and system scale.* A *workload* is a family of circuits specified by (i) the total logical width (number of data

qubits) and (ii) a two-qubit *interaction pattern* that determines which qubit pairs are considered for two-qubit gates. We consider three workload families commonly used in quantum benchmarking: (i) *Nearest-neighbor circuits*, where all two-qubit gates act on adjacent qubits in a 1D chain, representing highly local, hardware-friendly patterns; (ii) *Random Clifford+T circuits*, consisting of mixed single-qubit Cliffords, scattered CNOTs, and sparse  $T/T^{\dagger}$  gates, approximating generic fault-tolerant workloads with moderate non-locality; and (iii) *Long-range circuits*, where two-qubit gates couple uniformly random pairs of qubits, producing communication-heavy programs with high non-locality.

System size is the number of QPUs, denoted by  $N$ . The total circuit width is set proportional to system scale by assigning each QPU a fixed local grid of data qubits. We evaluate multiple *system scales* by varying  $N$  while keeping the per-QPU data-qubit capacity and the number of communication qubits per QPU fixed. Thus, increasing  $N$  increases the *total* circuit width proportionally (more QPUs, each with the same local qubit grid). The resulting circuits are then partitioned using the same compilation and mapping pipeline and simulated under architecture-specific routing and scheduling policies (we explain this later). Circuits are partitioned using a lightweight Kernighan–Lin (KL) heuristic [15]. For the *monolithic baseline*, we assume a single QPU that hosts all physical qubits required to handle the circuit, supports full all-to-all connectivity, and incurs no inter-QPU communication or entanglement-generation overhead. The circuit execution latency in this case is denoted by  $T_{\text{mono}}$ .

*Key physical parameters.* Here we define the key parameters that we change in the system. *Switch insertion loss* is the optical attenuation (in dB) incurred when a photon traverses a switching element. *Switch reconfiguration delay* is the time required to reconfigure an optical switch before it can support a new set of connections (e.g., setting up new optical paths in the network). *memory cutoff or memory coherence time* (or *coherence cutoff*) is denoted by  $\tau_{\text{cut}}$  and is the maximum time an entangled qubit may be stored at a QPU (e.g., at a repeater) before it is discarded. This parameter is only relevant for server-centric architectures (e.g., BCUBE).

*Execution model and schedulers.* We represent each quantum circuit as a directed acyclic graph (DAG), where nodes correspond to gates and edges encode dependencies between gates. At any time, there is a set of *ready* gates (called frontier layer) whose predecessors have all completed. We remove completed gates from the DAG, which may expose new ready gates and form the next frontier. For each DAG layer (frontier), we process the ready non-local gates in a random order. For each gate, the scheduler attempts to reserve the required communication resources by invoking

the path-selection procedure: it searches for a feasible qubit-to-qubit path. If a feasible path is found, the corresponding resources are reserved immediately; otherwise, the gate is deferred and remains in the frontier for the next scheduling step. We advance simulated time by the latency of the *slowest* successfully established remote entanglement in that layer (including switch reconfiguration delay), commit the completed gates, release their resources, and repeat the procedure for the next layer. After parsing and serving all the gates in the DAG, we report the final value of the time variable as circuit execution latency.

*Path selection and scheduling.* For each non-local two-qubit gate, the scheduler searches for a *shortest feasible qubit-to-qubit path* between the two QPUs that host the gate's operand qubits. Candidate paths are enumerated in increasing hop count order and tested sequentially. A path is feasible only if all required resources are available: sufficient capacity on each fabric edge (optical channels), sufficient communication qubits at the endpoint QPUs, and sufficient BSM resources. In switch-centric architectures (QFly, Clos, Fat-Tree), a multi-hop path requires only one BSM at the fabric to establish end-to-end entanglement. In BCube, entanglement is generated hop by hop: each intermediate QPU must have available communication qubits to act as a repeater, and each adjacent QPU pair requires BSM capacity at the connecting switch.

Among shortest feasible paths, the scheduler greedily selects the first valid candidate and immediately reserves the required resources. Circuit execution is driven by an event-based scheduler that uses expected EPR-generation latencies derived from stochastic loss and accounts for contention for BSMs and switch reconfiguration delays.

For a given distributed architecture, we denote the corresponding end-to-end execution latency by  $T_{\text{dist}}$ . We report results using the *distributed-to-monolithic latency ratio*

$$\rho_{\text{lat}} \triangleq \frac{T_{\text{dist}}}{T_{\text{mono}}}, \quad (8)$$

which isolates the performance overhead introduced purely by distribution and communication. Values of  $\rho_{\text{lat}}$  close to one indicate near-ideal scaling relative to the monolithic baseline, while larger values reflect increasing communication and scheduling overheads.

### 3.1 Sanity Checks: Remote-Gate Timing Under Varying Parameters

We begin by performing sanity checks to ensure that the simulator responds sensibly to basic physical trends. These experiments are not intended to validate the model but rather to verify that loss, retry, and storage effects behave as expected.

We consider paths with  $h = 4$  hops, where adjacent components (QPU–switch or switch–switch) are separated by 0.1 km, with fiber attenuation of 0.2 dB/km. Communication-qubit memory loss due to storage and swapping in the server-centric case is fixed at 3 dB per QPU. The EPR source rate is  $10^6$  pairs/s, and the local two-qubit gate time is  $T_{\text{local}} = 10 \mu\text{s}$ . Switch reconfiguration delay is excluded to isolate loss and memory effects.

For the Server-centric paradigm, we evaluate both **sequential** (S) and **parallel** (P) swap-scheduling protocols proposed in [24], with a memory cutoff time  $\tau_{\text{cut}}$  that limits how long a partially generated entangled state may be stored if the required swaps have not yet been completed, after which the attempt is discarded. We report two derived, dimensionless metrics to summarize the behavior of the optical loss and entanglement-timing model.

First, we define the *EPR-generation latency ratio* as

$$\rho_{\text{EPR}} \triangleq \frac{\mathbb{E}[T_{\text{pair}}]}{T_{\text{local}}}, \quad (9)$$

where  $\mathbb{E}[T_{\text{pair}}]$  is the expected latency to generate the end-to-end EPR pair required for executing a non-local two-qubit gate under the selected route and entanglement-generation protocol (cf. Eqs. (6)–(7)), and  $T_{\text{local}}$  is the duration of a local two-qubit gate. This ratio captures the relative cost of remote entanglement generation compared to local computation.

Second, we define the *switch-to-memory loss ratio* as

$$\rho_{\ell} \triangleq \frac{L_{\text{sw}}^{(\text{hop})}}{L_{\text{mem}}}, \quad (10)$$

where  $L_{\text{sw}}^{(\text{hop})}$  denotes the insertion loss incurred by a single switch traversal. Following a Beneš-style optical switch fabric, we approximate  $L_{\text{sw}}^{(\text{hop})} = (2\lceil \log_2 k \rceil - 1) \ell_{2 \times 2}$ , where  $k$  is the switch radix and  $\ell_{2 \times 2}$  is the loss of a single  $2 \times 2$  switching element. In this experiment, we fix the switch radix to  $k = 2$ , yielding  $L_{\text{sw}}^{(\text{hop})} = \ell_{2 \times 2}$ . The term  $L_{\text{mem}}$  is the per-hop memory-induced loss incurred when a QPU stores and swaps entanglement while acting as an intermediate repeater. This ratio characterizes the relative penalty of switch-centric versus server-centric entanglement distribution as path length increases.

Figure 6 reports the *EPR-generation latency ratio*  $\rho_{\text{EPR}} = \mathbb{E}[T_{\text{pair}}]/T_{\text{local}}$  for a fixed multi-hop path as a function of the *switch-to-memory loss ratio*  $\rho_{\ell} = L_{\text{sw}}^{(\text{hop})}/L_{\text{mem}}$ . In switch-centric architectures, photons traverse only the optical fabric, incurring switch insertion loss at every hop but avoiding memory-induced loss. In contrast, server-centric architectures incur fewer switch traversals but rely on intermediate QPUs to store and swap entanglement, making them sensitive to memory loss and coherence constraints.

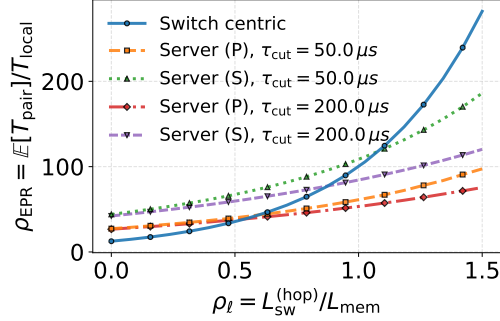


**Figure 6: EPR-generation latency ratio  $\rho_{\text{EPR}} = \mathbb{E}[T_{\text{pair}}]/T_{\text{local}}$  as a function of the per-hop switch-to-memory loss ratio  $\rho_l = L_{\text{sw}}^{(\text{hop})}/L_{\text{mem}}$  for a four-hop path. We compare switch-centric entanglement distribution with server-centric (QPU-assisted) sequential and parallel protocols under two communication-qubit coherence cutoffs. Server-centric paths incur fewer switch traversals and benefit from parallel EPR generation when coherence times are long, while switch-centric paths perform better when memory-induced loss dominates.**

When the communication-qubit coherence cutoff  $\tau_{\text{cut}}$  is small, server-centric paths experience frequent memory expiration events, inflating  $\mathbb{E}[T_{\text{pair}}]$  and degrading performance as explained in [24]. As  $\tau_{\text{cut}}$  increases (e.g., from  $50\ \mu\text{s}$  to  $200\ \mu\text{s}$ ), memory expirations are reduced and *parallel* entanglement generation protocols enable concurrent link establishment across hops, significantly lowering the expected EPR-generation latency relative to *sequential* protocols.

Conversely, when  $\rho_l$  approaches zero—i.e., when memory-induced loss dominates over switch insertion loss—switch-centric architectures outperform server-centric ones regardless of protocol choice, since server-centric paths incur an unavoidable memory-loss penalty from storing and retrieving entangled qubits.

### 3.2 Workload and Scale Sensitivity

This experiment evaluates how circuit execution latency varies across both workload structure and system scale for four representative quantum data-center architectures (QFly, BCube, and Fat-Tree, and Clos). We fix the underlying physical-layer parameters—including fiber attenuation, switch insertion loss, switch reconfiguration delay, and per-QPU data-qubit capacity—and examine two axes of variation: (i) the *type of circuit workload* and (ii) the *number of QPUs* in the system.

### 3.3 Architecture Instantiations

To enable a fair and reproducible comparison, we first describe how each quantum data-center architecture is instantiated for a given system size  $N$ . For each topology, we follow standard constructions from the literature and widely adopted best practices, selecting parameters that respect realistic switch port budgets, scale to the target number of QPUs, and align physical-layer assumptions across architectures as closely as possible. Where exact alignment is not feasible, we preserve architectural feasibility; for example, in BCube, forcing QPUs to have the same port count as in Fat-Tree can render the topology disconnected even with an arbitrarily large number of switches, and is therefore not imposed.

In our model, switch ports serve three distinct roles: (i) connecting switches to other switches, (ii) connecting switches to QPUs, and (iii) interfacing with BSM modules (Bell state analyzers and photon detectors) to perform entanglement swapping. To avoid conflating architectural topology with entanglement-generation resources such as BSAs and photon detectors, we first construct the logical network topology of each architecture using switch ports only for inter-switch and switch-QPU connectivity. BSM resources are incorporated *after* the topology is instantiated, allowing us to isolate the effects of classical network structure from the provisioning of quantum entanglement-generation resources.

We consider two complementary models for allocating BSM resources to switches. In the first model, we assume a *fixed number of BSMs per switch*. Under this assumption, once the topology of each architecture is instantiated, each switch is provisioned with additional ports dedicated to BSM modules, causing the total BSM budget to scale with the number of switches. This model isolates the impact of architectural structure when entanglement-generation capability is locally provisioned rather than globally constrained.

In the second model, we assume a *fixed total BSM budget* shared across the entire architecture. This budget is distributed evenly across all switches, implying that architectures with different numbers of switches receive different per-switch BSM allocations. As a result, architectures with fewer switches receive a higher number of BSMs per switch and therefore require more BSM-facing ports on each switch, while deeper or switch-rich architectures divide the same budget across a larger number of switching elements.

*Fat-Tree and Clos.* For Fat-Tree, we instantiate the topology using the parameterization and scaling equations introduced in Section 2, selecting the minimum feasible switch radix that supports the target system size  $N$ . The resulting Fat-Tree switch radix is then used as a common reference when parameterizing the QFly and BCube architectures, ensuring consistent port budgets across all evaluated topologies.

*Clos instantiation.* Following the design space described in Section 2, we instantiate Clos topologies using an automated layout procedure that derives a feasible configuration for each target system size  $N$ . The procedure selects an even switch radix  $k$ , determines the number of top-of-rack (ToR) switches  $T = k^2/4$ , and assigns the number of QPUs per rack  $R$  such that  $T \times R \geq N$ , while respecting practical constraints on rack fanout and ToR port budgets. This construction follows the standard folded-Clos model, where each ToR switch allocates  $k/2$  ports to QPUs and  $k/2$  ports to uplinks [7, 9, 28].

To reflect different points in the Clos design space, we use two instantiation policies. *Clos\_tight* prioritizes minimizing unused rack capacity ( $T \times R - N$ ), yielding densely packed racks. *Clos\_compact* prioritizes minimizing the total number of switches, allowing limited unused rack capacity when this significantly reduces fabric size. For each policy, once  $(k, T, R)$  is determined, the aggregation and core layers, inter-stage connectivity, and path structure are derived deterministically.

*QFly.* QFly is instantiated under the same per-switch port budget  $k$  as the Fat-Tree baseline. Each switch devotes  $m = k/2$  ports to attached QPUs, matching the Fat-Tree edge fanout.

Let  $S$  denote the number of QFly switches and define  $k_{\text{ring}}$  as the number of inter-switch ports per switch. We consider three QFly variants that differ in how inter-switch connectivity is realized:

- *QFly* ( $k_{\text{ring}} = m/2$ ): With  $m = k/2$  ports allocated to QPUs, only  $m/2$  ports per switch are used for inter-switch connectivity, yielding partial connectivity among switches.
- *QFly* ( $k_{\text{ring}} = k - m$ ): With  $m = k/2$  ports reserved for QPU attachment, all remaining  $k - m$  ports per switch are used for inter-switch connectivity, maximizing switch-level path diversity under a fixed port budget.
- *QFly* ( $k_{\text{ring}} = N/m - 1$ ): Switches are assumed to be fully connected, corresponding to an idealized upper bound that exceeds the original port budget.

*BCube.* : We instantiate BCube using the same port budget as Fat-Tree by setting  $n \triangleq k$ . We choose the smallest  $k_{\text{bcube}}$  such that:

$$k_{\text{bcube}} = \lceil \log_n(N) \rceil - 1. \quad (11)$$

BCube has  $L = k_{\text{bcube}} + 1$  switch levels; each level contains  $n^{k_{\text{bcube}}}$  switches:

$$S_{\text{per-level}} = n^{k_{\text{bcube}}}, \quad S_{\text{total}} = (k_{\text{bcube}} + 1) n^{k_{\text{bcube}}}. \quad (12)$$

Table 4 summarizes the derived architectural parameters used in the experiments. For each architecture and QPU count, the table reports the total number of switches, the number of QPUs per rack (or edge switch), and the number of

**Table 3: Fixed physical and system parameters used in the workload scalability experiment.**

Parameter	Value
QPU capacity (data qubits per QPU)	16
Communication qubits per QPU	5
Optical channels per fiber	5
QPU–switch distance	0.1 km
Switch–switch distance	0.1 km
Fiber attenuation	0.1 dB/km
Communication-qubit memory loss	3 dB
Switch insertion loss	0.3 dB
Communication-qubit reset time	$T_{\text{reset}} = 10 \mu\text{s}$
EPR source generation rate	$10^6 \text{ pairs/s}$
Coherence cutoff (BCube)	$\tau_{\text{cut}} = 200 \mu\text{s}$
Total BSM budget	100

available BSMs per switch. These parameters are determined by the topology construction rules of each architecture (e.g., Clos layers, BCube levels, or QFly rings) and are not independently tuned. As a result, the table reflects the inherent scaling properties of each architecture rather than additional optimization.

As an example, consider BCube scaling from  $N = 64$  to  $N = 128$  QPUs. We derive the per-switch port budget  $k_{\text{FT}}$  from the Fat-Tree baseline as  $k_{\text{FT}} = \lceil (4N)^{1/3} \rceil$ , rounded to the next even integer, which yields  $k_{\text{FT}} = 8$ . In the  $(n, k)$ -BCube construction, we set  $n = k_{\text{FT}}$  and choose  $k = \lceil \log_n N \rceil - 1$ , giving  $k = 1$  for  $N = 64$  and  $k = 2$  for  $N = 128$ . For  $N = 64$ , this yields two switch levels, and since QPU identifiers occupy only a single value of the most significant base- $n$  digit, only 16 switches are active. For  $N = 128$ , the additional level activates a third layer of switches; although the total fabric contains  $(k + 1)n^k = 192$  switches, only those connected to at least one QPU are active, resulting in 16, 16, and 64 active switches across the three levels, for a total of 96. The jump in switch count from 16 to 96 therefore arises from a configuration boundary in BCube, where increasing  $N$  forces the introduction of an additional level in the multi-stage fabric.

For Fig. 7, *fixed BSMs-per-switch* model, where each switch is provisioned with exactly two BSMs, causing the total BSM budget to scale with the number of switches. In contrast, Fig. ?? adopts a fixed global budget of BSMs that is evenly distributed across all switches in each architecture. All fixed parameters for this experiment are summarized in Table 3. Unlike approaches that restrict BSM placement to specific layers, we distribute BSM resources across *all* switch layers in the instantiated topology.

Arch.	#QPUs	#Sw.	QPUs/Rack	Ports/Sw.	#ToRs
QFly ( $k_{\text{ring}} = N/m - 1$ )	16	8	2.00	9/9	8
QFly ( $k_{\text{ring}} = m/2$ )	16	8	2.00	6/6	8
QFly ( $k_{\text{ring}} = k - m$ )	16	8	2.00	4/4	8
Clos_tight	16	28	1.00	8.00	16
Clos_compact	18	18	2.00	6.00	9
Fat-Tree	16	20	2.00	4.00	8
BCube	16	8	2.00	4.00	8
QFly ( $k_{\text{ring}} = N/m - 1$ )	64	16	4.00	19/19	16
QFly ( $k_{\text{ring}} = m/2$ )	64	16	4.00	12/12	16
QFly ( $k_{\text{ring}} = k - m$ )	64	16	4.00	8/8	16
Clos_tight	64	28	4.00	8.00	16
Clos_compact	64	28	4.00	8.00	16
Fat-Tree	64	80	4.00	8.00	32
BCube	64	16	4.00	8.00	16
QFly ( $k_{\text{ring}} = N/m - 1$ )	128	32	4.00	35/35	32
QFly ( $k_{\text{ring}} = m/2$ )	128	32	4.00	20/20	32
QFly ( $k_{\text{ring}} = k - m$ )	128	32	4.00	8/8	32
Clos_tight	128	88	2.00	16.00	64
Clos_compact	150	40	6.00	10.00	25
Fat-Tree	128	80	4.00	8.00	32
BCube	128	96	1.33	8.00	96

**Table 4: Topology summary across architectures and system scales.** #QPUs denotes the total number of QPUs supported by the instantiated fabric. #Sw. is the total number of active switches across all layers. #ToRs is the number of top-of-rack (edge) switches. QPUs/Rack reports the maximum number of QPUs attached to any ToR. Ports/Sw. reports the maximum switch degree; for QFly, input/output ports are reported separately. BCube does not have a meaningful rack abstraction, and QPUs/Rack reflects the effective attachment multiplicity.

*Scaling the number of QPUs.* To assess scalability, we repeat the experiment for increasing system sizes (e.g.,  $N \in \{8, 16, 32, 64, 128\}$  QPUs). For each architecture and QPU count, we generate a circuit from the selected workload family with the number of two-qubit gates scaled with  $N$  (ranging from 200 at  $N=8$  to 600 at  $N=128$ ), partition it across the available QPUs using the same compilation pipeline, and simulate its distributed execution. We report scalability using the distributed-to-monolithic latency ratio  $\rho_{\text{lat}}$ , which captures how execution latency grows with system size relative to the monolithic baseline.

*Fixed BSMs per switch.* Figure 7 shows the distributed-to-monolithic latency ratio  $\rho_{\text{lat}} = T_{\text{dist}}/T_{\text{mono}}$  when the number of BSMs is fixed per switch. Results are reported *separately for each workload*, with each bar representing the average over 50 independent runs. Across all architectures, the latency ratio generally increases with system size, as a larger fraction of two-qubit gates must be executed remotely. This effect is most pronounced for the long-range workload

(Fig. 7c), which places the heaviest demand on the interconnect, while the nearest-neighbor workload (Fig. 7a) remains nearly flat since most operations can be executed locally. Under this model, architectures with many switches benefit from a larger aggregate BSM budget: clos\_tight and Fat-Tree achieve the lowest latency ratios, with clos\_compact slightly worse. QFly remains competitive but does not dominate, as its small switch footprint limits the total BSM budget. BCube’s behavior is more parameter-dependent, influenced by the coherence cutoff and by whether QPUs act as repeaters, which introduce additional memory and swap overhead. We will explore this later in this section. Note that in some cases increasing the number of QPUs also exposes additional parallelism that can partially offset the higher gate count, leading to small local decreases in the ratio.

*Fixed total BSM budget.* For the fixed-total-BSM model, we focus exclusively on the long-range workload, as it represents the most communication-intensive setting. When the global BSM budget is held constant and evenly distributed across switches, architectures with fewer switches receive a larger per-switch share of resources (here BSMs), reversing the scaling advantage. In this regime, QFly performs best overall as shown in figure 8, with the fully connected variant ( $k_{\text{ring}} = N/m - 1$ ) achieving the lowest latency ratios across scales. Even under port-feasible configurations ( $k_{\text{ring}} = m/2$ ), QFly consistently outperforms Clos and Fat-Tree. In contrast, Clos and Fat-Tree spread the fixed budget over many more switches, increasing contention; this effect compounds with their longer multi-stage paths and higher entanglement-generation latency as shown in Fig. 9.

**3.3.1 Path Hop-Count Distribution of Non-Local Gates.** We next examine architectural differences by analyzing the hop-count distribution of paths used to serve non-local gates when the number of BSMs is fixed per switch. Figure 9 reports the fraction of non-local gates as a function of path length for systems with 32 and 128 QPUs across architectures.

As system size increases from 32 to 128 QPUs, all architectures exhibit a shift toward longer paths. Notably, in switch-centric architectures such as Fat-Tree and both Clos variants, a larger fraction of non-local gates are served over six-hop paths than in BCube at 128 QPUs. Despite this increase in hop count, Fat-Tree and Clos experience only a modest increase in the distributed-to-monolithic latency ratio (Fig. 7c).

In contrast, BCube exhibits a substantially larger latency increase even though its hop-count distribution is comparable to that of switch-centric designs. The key reason lies in how hops are realized. In BCube, paths longer than two hops necessarily traverse intermediate QPUs acting as repeaters, so each hop incurs quantum-memory loss and requires an additional Bell-state measurement for entanglement swapping.

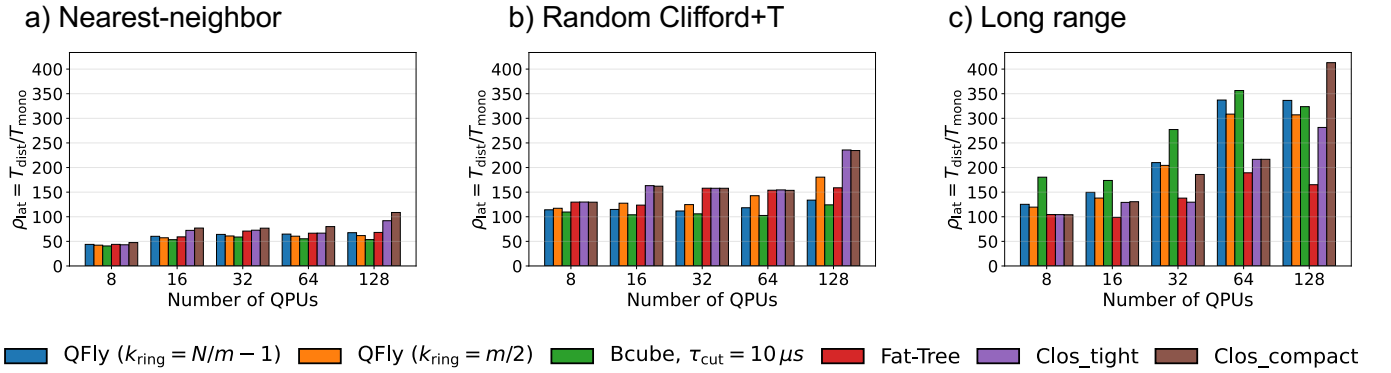


Figure 7: Latency ratio (Distributed / Monolithic) versus number of QPUs for each workload under the *fixed BSMs per switch* resource model. Bars show the average ratio across repeated runs for all architectures present in the dataset. Lower values indicate better scalability relative to the monolithic baseline.

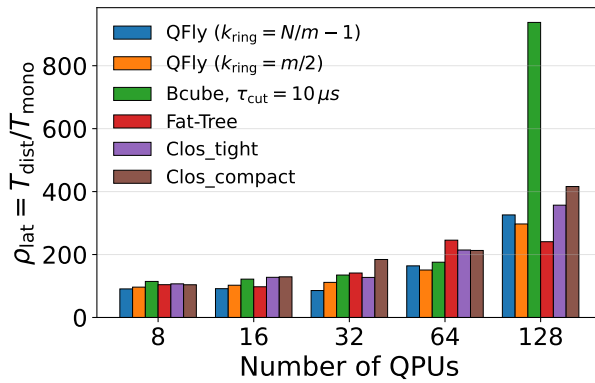


Figure 8: Latency ratio (Distributed / Monolithic) versus number of QPUs under the *total BSMs budget* resource model for the long-range workload. Bars show the average ratio across repeated runs for all evaluated architectures. Lower values indicate better scalability relative to the monolithic baseline.

In our model, this corresponds to a per-hop memory loss of 3 dB, compared to 0.3 dB per switch traversal in switch-centric architectures. This accumulated memory loss significantly increases the expected EPR-generation latency and amplifies the performance penalty at larger scales.

By contrast, switch-centric architectures establish end-to-end entanglement using a single BSM along the path and avoid intermediate quantum memory, making their latency substantially less sensitive to increased hop count. While this behavior is intrinsic to the server-centric design of BCube, it suggests that BCube-specific scheduling and swap-coordination algorithms could mitigate part of this overhead.

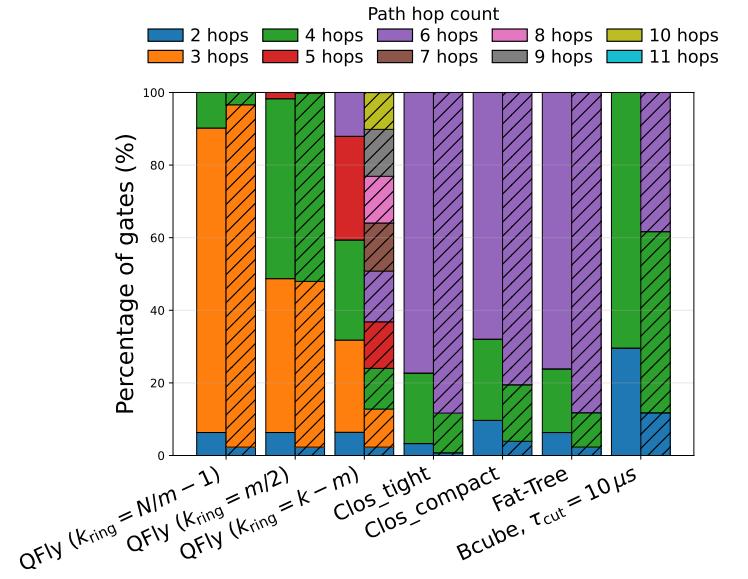
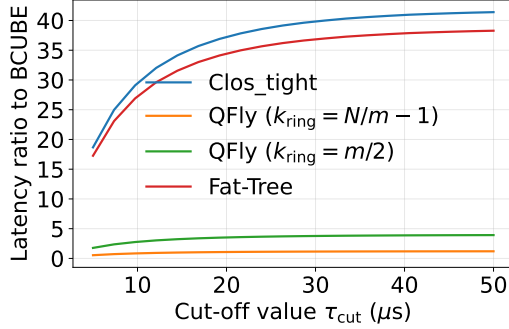


Figure 9: Fraction of non-local gates served over paths of different hop counts for 32- and 128-QPU configurations across the evaluated architectures. Solid rectangles correspond to 32 QPUs, while dashed rectangles correspond to 128 QPUs.

### 3.4 Sensitivity of BCube to communication qubits coherence time

Next, we study the impact of the cutoff time parameter  $\tau_{\text{cut}}$  on distributed circuit execution latency by comparing different quantum data-center architectures relative to the BCube architecture. As discussed earlier, entanglement-swap scheduling protocol and the duration for which partially generated



**Figure 10: Latency ratio of switch-centric architectures to BCUBE as a function of the cut-off value  $\tau_{\text{cut}}$  under the parallel swap scheduling protocol for 128 QPUs, 5 communication qubits per QPU and total BSM budget of 100 evenly distributed among switches.**

entanglement can be retained in memory before being discarded can affect the performance of server-centric architectures. Throughout this section, we use the terms *coherence time* and *cutoff time* interchangeably, as both refer to this memory-lifetime constraint.

In this experiment, we fix the circuit and network configuration (long-range workload, fixed number of QPUs, communication qubits, and BSM allocation), set the cutoff time  $\tau_{\text{cut}}$  in the BCUBE network model, simulate distributed circuit execution, and record the resulting execution latency. For BCUBE, we use the parallel swap scheduling protocol proposed in [24].

Figure 10 shows the latency ratio of each architecture relative to BCUBE as a function of the communication-qubit memory cutoff value  $\tau_{\text{cut}}$ . The cutoff value controls how long an entangled state generated on any *entanglement segment*—defined here as a single QPU–switch–QPU link—can be stored in quantum memory before being discarded if entanglement on the remaining segments of the path has not yet been established. In BCUBE, non-local operations often require multi-hop paths composed of multiple such segments (e.g., a four-hop path consisting of two QPU–switch–QPU segments), where entanglement generation on different segments proceeds in parallel and may complete at different times. A larger  $\tau_{\text{cut}}$  allows early-completing segments to wait longer for the remaining segments to succeed, increasing the probability that all segments are simultaneously available and reducing the expected entanglement-generation latency. As a result, BCUBE performance improves steadily as  $\tau_{\text{cut}}$  increases, leading to an increasing latency ratio of switch-centric architectures relative to BCUBE.

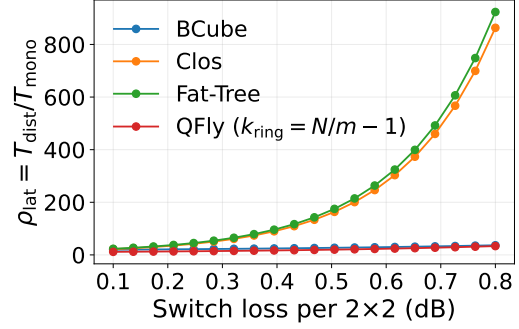


**Figure 11: Latency ratio versus per-switch insertion loss, showing higher sensitivity for deeper switch-centric architectures (Clos and Fat-Tree) compared to QFly and BCUBE.**

### 3.5 Switch Improvements vs. Circuit Execution Latency

We now report the results of the switch-loss sensitivity experiment. For each architecture, we fix the workload (*long\_range*) and all non-loss parameters (including a fixed switch reconfiguration duration), and directly sweep the switch insertion loss per  $2 \times 2$  element,  $\ell_{2 \times 2}$ , over a practical range. For each loss configuration, we run the distributed circuit execution, evaluate the resulting end-to-end execution latency using our physical-layer entanglement timing model, and report the latency ratio (distributed / monolithic) averaged over repeated runs.

*Observations.* Figure 11 shows that increasing switch insertion loss monotonically worsens the latency ratio for all architectures. However, the degradation is substantially steeper for Clos and Fat-Tree than for QFly and BCUBE. The underlying reason is architectural: deeper switch-centric designs (Clos and Fat-Tree) realize remote entanglement over paths that traverse a larger number of optical switches, so increasing  $\ell_{2 \times 2}$  accumulates loss more aggressively along the path, reducing the success probability of each attempt and inflating the expected EPR-generation latency.

In contrast, QFly typically achieves remote connectivity with fewer switch traversals, making it less sensitive to the same per-switch loss increase. BCUBE is also comparatively less sensitive in this sweep because some intermediate nodes on its entanglement paths are *QPUs acting as repeaters*, which we do not model as contributing switch insertion loss; thus, raising  $\ell_{2 \times 2}$  does not penalize those hops. (We keep the repeater memory-loss parameter fixed throughout this experiment, so the observed trends isolate the impact of switch insertion loss.)

## 4 Conclusion and Discussion

We presented a systematic benchmarking study of QDC architectures for DQC, quantifying how topology, scheduling, and physical-layer constraints jointly determine end-to-end circuit execution latency. Across multiple QFly variants, BCube, Clos, and Fat-Tree, and under realistic entanglement-generation models and diverse workloads, our results show that distributed quantum performance cannot be inferred from topology alone: it emerges from the interaction of multiple factors including path structure, switching resources, and coherence-limited entanglement dynamics.

Our evaluation exposes clear architectural trade-offs. Switch-centric fabrics (QFly/Clos/Fat-Tree) avoid using QPUs as repeaters, reducing sensitivity to communication-qubit coherence cutoffs, but they incur switch loss on every hop and can become bottlenecked by contention for shared BSM resources—especially in deeper hierarchies with longer end-to-end paths. In contrast, the server-centric BCube design can exploit shorter effective paths and QPU-assisted swapping, but its latency grows with scale when repeater chains become longer and performance becomes sensitive to finite retry windows and memory-induced loss on intermediate QPUs. Across all architectures, hop count is a primary driver of both optical-loss accumulation and expected EPR generation time, and thus a key determinant of scalability on communication-heavy workloads.

Our sensitivity experiments further show that hardware improvements yield architecture-dependent benefits. Increasing switch insertion loss degrades latency ratios for all designs, but the penalty is substantially steeper for switch-rich, multi-stage fabrics (Clos/Fat-Tree) because remote entanglement paths traverse more switches; QFly, with fewer switch traversals, is less sensitive, and BCube is comparatively less affected because intermediate QPU repeaters are not modeled as incurring switch insertion loss in those hops (with memory-loss held fixed in that sweep).

These results suggest several directions for co-design. First, topology should be chosen and parameterized jointly with BSM placement and scheduling: path diversity only translates into latency gains when the scheduling policy can exploit it under realistic BSM contention. Second, physical-layer control knobs (coherence windows, retry policies, and switch configuration strategies) should be exposed to the scheduler and tuned to workload structure, since long-range workloads amplify sensitivity to hop count, loss, and shared resources. Finally, future QDC platforms will likely require cross-layer optimization that couples architectural design (diameter and switch footprint), orchestration (routing and contention-aware scheduling), and photonic hardware choices (loss, switching latency, and detector/BSM provisioning) to achieve robust scaling for DQC.

Overall, our study provides quantitative guidance for designing scalable quantum data centers and establishes a benchmarking foundation for evaluating emerging QDC architectures and future fault-tolerant distributed execution stacks.

## 5 Acknowledgements

The authors acknowledge insightful discussions with Amin Taherkhani, Jiapeng Zhao, Narges Alavisamani, and Ramin Ayanzadeh.

## References

- [1] Mohammad Al-Fares, Alexander Loukissas, and Amin Vahdat. 2008. A Scalable, Commodity Data Center Network Architecture. In *Proceedings of the ACM SIGCOMM Conference*. 63–74.
- [2] Mohammad Al-Fares, Alexander Loukissas, and Amin Vahdat. 2008. A scalable, commodity data center network architecture. *ACM SIGCOMM computer communication review* 38, 4 (2008), 63–74.
- [3] Jonathan M Baker, Casey Duckering, Alexander Hoover, and Frederic T Chong. 2020. Time-sliced quantum circuit partitioning for modular architectures. In *Proceedings of the 17th ACM International Conference on Computing Frontiers*. 98–107.
- [4] Hans KC Beukers, Matteo Pasini, Hyeongrak Choi, Dirk Englund, Ronald Hanson, and Johannes Borregaard. 2024. Remote-entanglement protocols for stationary qubits with photonic interfaces. *PRX Quantum* 5, 1 (2024), 010202.
- [5] Felix Burt, Kuan-Cheng Chen, and Kin K Leung. 2024. Generalised circuit partitioning for distributed quantum computing. In *2024 IEEE International Conference on Quantum Computing and Engineering (QCE)*, Vol. 2. IEEE, 173–178.
- [6] J Ignacio Cirac, AK Ekert, Susana F Huelga, and Chiara Macchiavello. 1999. Distributed quantum computation over noisy channels. *Physical Review A* 59, 6 (1999), 4249.
- [7] Charles Clos. 1953. A Study of Non-Blocking Switching Networks. *Bell System Technical Journal* 32, 2 (1953), 406–424.
- [8] Daniele Cuomo, Marcello Caleffi, Kevin Krsulich, Filippo Tramonto, Gabriele Agliardi, Enrico Prati, and Angela Sara Cacciapuoti. 2023. Optimized compiler for distributed quantum computing. *ACM Transactions on Quantum Computing* 4, 2 (2023), 1–29.
- [9] Albert Greenberg, James Hamilton, Navendu Jain, Srikanth Kandula, Changhoon Kim, Parantapa Lahiri, David A. Maltz, Parveen Patel, and Sudipta Sengupta. 2009. VL2: A Scalable and Flexible Data Center Network. In *Proceedings of the ACM SIGCOMM Conference*. 51–62.
- [10] Chuanxiong Guo, Guohan Lu, Dan Li, Haitao Wu, Xuan Zhang, Yunfeng Shi, Chen Tian, Yongguang Zhang, and Songwu Lu. 2009. BCube: a high performance, server-centric network architecture for modular data centers. In *Proceedings of the ACM SIGCOMM 2009 conference on Data communication*. 63–74.
- [11] Chuanxiong Guo, Haitao Wu, Kun Tan, Lei Shi, Yongguang Zhang, and Songwu Lu. 2008. Dcell: a scalable and fault-tolerant network structure for data centers. In *Proceedings of the ACM SIGCOMM 2008 conference on Data communication*. 75–86.
- [12] Dominic Horsman, Austin G Fowler, Simon Devitt, and Rodney Van Meter. 2012. Surface code quantum computing by lattice surgery. *New Journal of Physics* 14, 12 (2012), 123011.
- [13] Liang Jiang, Jacob M Taylor, Anders S Sørensen, and Mikhail D Lukin. 2007. Distributed quantum computation based on small quantum registers. *Physical Review A—Atomic, Molecular, and Optical Physics* 76, 6 (2007), 062323.

[14] Eneet Kaur, Shahrooz Pouryousef, Hassan Shapourian, Jiapeng Zhao, Michael Kilzer, Ramana Kompella, and Reza Nejabati. 2025. Optimized quantum circuit partitioning across multiple quantum processors. *IEEE Transactions on Quantum Engineering* (2025).

[15] B. W. Kernighan and S. Lin. 1970. An efficient heuristic procedure for partitioning graphs. *The Bell System Technical Journal* 49, 2 (1970), 291–307. doi:10.1002/j.1538-7305.1970.tb01770.x

[16] Batuhan Keskin, Cameron Afradi, Sylvain Lovis, Maurizio Palesi, Pau Escofet, Carmen G Almudever, and Edoardo Charbon. 2025. Lattice Surgery Aware Resource Analysis for the Mapping and Scheduling of Quantum Circuits for Scalable Modular Architectures. *arXiv preprint arXiv:2511.21885* (2025).

[17] John Kim, William J Daily, Steve Scott, and Dennis Abts. 2008. Technology-driven, highly-scalable dragonfly topology. *ACM SIGARCH Computer Architecture News* 36, 3 (2008), 77–88.

[18] Charles E. Leiserson. 1985. Fat-Trees: Universal Networks for Hardware-Efficient Supercomputing. *IEEE Trans. Comput.* C-34, 10 (1985), 892–901.

[19] Jan Li, Tim Coopmans, Patrick Emonts, Kenneth Goodenough, Jordi Tura, and Evert van Nieuwenburg. 2025. Optimising entanglement distribution policies under classical communication constraints assisted by reinforcement learning. *Machine Learning: Science and Technology* 6, 3 (2025), 035024.

[20] Yang Liu, Jogesh K Muppala, Malathi Veeraraghavan, Dong Lin, and Mounir Hamdi. 2013. *Data center networks: Topologies, architectures and fault-tolerance characteristics*. Springer Science & Business Media.

[21] D Main, P Drmota, DP Nadlinger, EM Ainley, A Agrawal, BC Nichol, R Srinivas, G Araneda, and DM Lucas. 2025. Distributed quantum computing across an optical network link. *Nature* (2025), 1–6.

[22] Christopher Monroe, Robert Raussendorf, Alex Ruthven, Kenneth R Brown, Peter Maunz, L-M Duan, and Jungsang Kim. 2014. Large-scale modular quantum-computer architecture with atomic memory and photonic interconnects. *Physical Review A* 89, 2 (2014), 022317.

[23] Lucian Popa, Sylvia Ratnasamy, Gianluca Iannaccone, Arvind Krishnamurthy, and Ion Stoica. 2010. A cost comparison of datacenter network architectures. In *Proceedings of the 6th International Conference*. 1–12.

[24] Shahrooz Pouryousef, Hassan Shapourian, and Don Towsley. 2024. Minimal Protocols for Entanglement Distribution with Finite Memory Coherence Time. In *2024 International Conference on Quantum Communications, Networking, and Computing (QCNC)*. IEEE, 150–159.

[25] Daisuke Sakuma, Amin Taherkhani, Tomoki Tsuno, Toshihiko Sasaki, Hikaru Shimizu, Kentaro Teramoto, Andrew Todd, Yosuke Ueno, Michal Hajdušek, Rikizo Ikuta, et al. 2024. An optical interconnect for modular quantum computers. *arXiv preprint arXiv:2412.09299* (2024).

[26] Hassan Shapourian, Eneet Kaur, Troy Sewell, Jiapeng Zhao, Michael Kilzer, Ramana Kompella, and Reza Nejabati. 2025. Quantum data center infrastructures: A scalable architectural design perspective. *arXiv preprint arXiv:2501.05598* (2025).

[27] Josiah Sinclair, Joshua Ramette, Brandon Grinkemeyer, Dolev Bluvstein, Mikhail D Lukin, and Vladan Vuletić. 2025. Fault-tolerant optical interconnects for neutral-atom arrays. *Physical Review Research* 7, 1 (2025), 013313.

[28] Arjun Singh, Joon Ong, Amit Agarwal, Glen Anderson, Ashby Armistead, Roy Bannon, Seb Boving, Gaurav Desai, Bob Felderman, Paul Germano, et al. 2015. Jupiter Rising: A Decade of Clos Topologies and Centralized Control in Google’s Datacenter Network. In *Proceedings of the ACM SIGCOMM Conference*. 183–197.

[29] Ron A Spanke and VE Benes. 1987. N-stage planar optical permutation network. *Applied Optics* 26, 7 (1987), 1226–1229.

[30] George Watkins, Hoang Minh Nguyen, Keelan Watkins, Steven Pearce, Hoi-Kwan Lau, and Alexandru Paler. 2024. A high performance compiler for very large scale surface code computations. *Quantum* 8 (2024), 1354.

[31] Wenfeng Xia, Peng Zhao, Yonggang Wen, and Haiyong Xie. 2016. A survey on data center networking (DCN): Infrastructure and operations. *IEEE communications surveys & tutorials* 19, 1 (2016), 640–656.

[32] Hezi Zhang, Yiran Xu, Haotian Hu, Keyi Yin, Hassan Shapourian, Jiapeng Zhao, Ramana Rao Kompella, Reza Nejabati, and Yufei Ding. 2025. SwitchQNet: Optimizing Distributed Quantum Computing for Quantum Data Centers with Switch Networks. In *Proceedings of the 52nd Annual International Symposium on Computer Architecture*. 1449–1463.